Topological dynamics of vortex-line networks in hexagonal manganites

Fei Xue, Nan Wang, Xueyun Wang, Yanzhou Ji, Sang-Wook Cheong, and Long-Qing Chen

Phys. Rev. B **97**, 020101 — Published 16 January 2018

DOI: 10.1103/PhysRevB.97.020101

Topological Dynamics of Vortex Line Networks in Hexagonal Manganites

Fei Xue,[1,*] Nan Wang,[1] Xueyun Wang,[2,3] Yanzhou Ji,[1] Sang-Wook Cheong,[3] and Long-Qing Chen[1]

[1]Department of Materials Science and Engineering, The Pennsylvania State University, University Park, Pennsylvania 16802, USA

[2]School of Aerospace Engineering, Beijing Institute of Technology, Beijing 100081, China

[3]Rutgers Center for Emergent Materials and Department of Physics and Astronomy, Rutgers University, Piscataway, NJ 08854, USA

*Corresponding author: xuefei5376@gmail.com

The 2D XY model is the first well-studied system with topological point defects. On the other hand, although topological line defects are common in 3D systems, the evolution mechanism of line defects is not fully understood. The six domains in hexagonal manganites converge to vortex lines in three dimensions. Using phase-field simulations, we predicted that during the domain coarsening process, the vortex line network undergoes three types of basic topological changes, i.e., vortex line loop shrinking, coalescence, and splitting. It is shown that the vortex-antivortex annihilation controls the scaling dynamics.

Spontaneous symmetry breaking may give rise to a special class of defects, called topological defects [1,2]. A topological defect is insensitive to small perturbations, and cannot be continuously de-tangled to the uniform distribution of order parameters. Topological defects are ubiquitous in different systems, ranging from the cosmological-scale topological defects in the early stage universe [3], vortices in type-II superconductors [4], disclinations in liquid crystals [5], to the vortex domains in solid functional materials [6]. The first well-studied system that shows topological defects is the XY model with the continuous U(1) symmetry, which possesses topological point defects in a two-dimensional (2D) space [1,7]. The point defects can be viewed as quasiparticles, two of which tangled in opposite ways can be annihilated when close to each other. On the other hand, although topological line defects are frequently observed in 3D bulk materials [6], little understanding of the topological evolution of line defects has been achieved.

Recently hexagonal (*h*-) $REMnO_3$ (RE, rare earths) have attracted significant attention due to their intriguing cloverleaf-like ferroelectric domains and topological defects [8-10]. In *h*-$REMnO_3$, the phase transition from space group $P6_3/mmc$ to $P6_3cm$ leads to a structural trimerization [8,11]. Different choices of the origin give rise to three translational phase variants, and each variant has two degenerate polar states with polarization along either $+c$ or $-c$ directions [11-14]. Thus, totally six energy-degenerate domains exist in the *h*-$REMnO_3$ systems. The coexistence of the six domains leads to the formation of 1D and 0D topological defects, i.e., vortex lines in 3D spaces and vortices/antivortices in 2D spaces (the vortices and anti-vortices are categorized based on the cycling sequence of the six domains around the cores) [8,9,15]. The cloverleaf-like domains and topological defects in *h*-$REMnO_3$ can be easily observed and analyzed at room temperature [16], which provides a unique opportunity to explore the evolution mechanism of topological line defects.

In this Letter, we report the evolution and interactions of topological line networks in *h*-$REMnO_3$ using the phase-field method with input directly from existing density functional theory calculations in the literature [10,17,18]. The phase-field simulations reveal that the topological defects in *h*-$REMnO_3$ are true vortices with the core region adopting the continuous U(1) symmetry. During the domain coarsening process, the evolution of the vortex lines involves three basic topological changes, i.e., shrinking and disappearance of vortex line loops, coalescence of smaller vortex line loops to form larger loops, and splitting of a vortex line loop into two loops. It is also shown that the vortex-antivortex annihilation rather than the domain wall motion controls the domain coarsening scaling dynamics.

Different *h*-$REMnO_3$ systems exhibit similar phase transitions and the same topological defects [16,19], and here we employ *h*-$YMnO_3$ as a representative example. In *h*-$YMnO_3$, the structural trimerization, the primary order parameter, is caused by the in-plane displacements of related oxygen atoms, and can be described by the magnitude Q and azimuthal angle Φ [10]. In the phase-field simulations, we transform the polar coordinates Q and Φ into Cartesian coordinates (Q_x, Q_y), with $Q_x = Q\cos\Phi, Q_y = Q\sin\Phi$. As an improper ferroelectric, *h*-$YMnO_3$ also exhibits an induced polarization P_z. Based on its hexagonal symmetry, the total free energy density is expressed as [10,18,20]

$$
\begin{aligned}
f = {} & \frac{a}{2}(Q_x^2+Q_y^2)+\frac{b}{4}(Q_x^2+Q_y^2)^2+\frac{c}{6}(Q_x^2+Q_y^2)^3+\frac{c'}{6}(Q_x^6-15Q_x^4Q_y^2+15Q_x^2Q_y^4-Q_y^6) \\
& -g(Q_x^3-3Q_xQ_y^2)P_z+\frac{g'}{2}(Q_x^2+Q_y^2)P_z^2+\frac{a_P}{2}P_z^2+\frac{s_Q^x}{2}[(\frac{\partial Q_x}{\partial x})^2+(\frac{\partial Q_x}{\partial y})^2+(\frac{\partial Q_y}{\partial x})^2+(\frac{\partial Q_y}{\partial y})^2] \quad (1) \\
& +\frac{s_Q^z}{2}[(\frac{\partial Q_x}{\partial z})^2+(\frac{\partial Q_y}{\partial z})^2]+\frac{s_P^z}{2}(\frac{\partial P_z}{\partial z})^2+\frac{s_P^x}{2}[(\frac{\partial P_z}{\partial x})^2+(\frac{\partial P_z}{\partial y})^2]-E_zP_z-\frac{1}{2}\varepsilon_0\kappa_bE_zE_z,
\end{aligned}
$$

where $a, b, c, c', g, g',$ and a_P are coefficients for the bulk free energy, s_Q^x, s_Q^z, s_P^x, and s_P^z are coefficients for the gradient energy terms, ε_0 is the vacuum permittivity, κ_b is the background dielectric constant [21], and E_z is the electric field calculated by $E_z = -\frac{\partial \varphi}{\partial z}$ with φ the electrostatic potential. The coefficients for the bulk free energy and gradient energy are obtained from first-principles calculations at 0 K as listed in Ref. [10], except that s_P^x is changed from $-8.88\ eV$ to $8.88\ eV$. As demonstrated in Supplementary Fig. S1 [22], the modification makes negligible changes to the primary order parameter profiles near the domain wall. However, this modification allows us to use the classical semi-implicit method to solve the time-dependent Ginzburg-Landau (TDGL) equations more efficiently [23]. Based on the assumption of Landau theory, the coefficient a should be temperature dependent as in Refs. [24,25]. However, this letter focuses on the topological changes and scaling dynamics, which are insensitive of the magnitude of order parameters. Therefore, all the coefficients are assumed to be temperature independent. The background dielectric constant κ_b is assumed to take the typical value of 50 [26].

The domain structures are evolved by solving the TDGL equations

$$\frac{\delta P_z}{\delta t} = -L_P \frac{\delta f}{\delta P_z}, \frac{\delta Q_x}{\delta t} = -L_Q \frac{\delta f}{\delta Q_x}, \frac{\delta Q_y}{\delta t} = -L_Q \frac{\delta f}{\delta Q_y}, \tag{2}$$

where L_P and L_Q are the kinetic coefficients related to the domain wall mobility. The TDGL equations assume that the changing rate of order parameters is proportional to the variational derivative of the total free energy of an inhomogeneous system with respect to the spatial distribution of order parameters. The TDGL equations are solved based on the semi-implicit

spectral method [23], and it is assumed that $L_P = L_Q = 0.05\, arb.unit$ in the simulations. The gradient energy coefficients are normalized based on $s_Q^{*z} = s_Q^{z} / g_0$, $s_Q^{*x} = s_Q^{*x} / g_0$, $s_P^{*z} = s_P^{*z} / g_0$, and $s_P^{*x} = s_P^{*x} / g_0$, where $g_0 = a(\Delta x)^2$. Thus the normalized gradient energy coefficients are determined by the grid spacing. Unless stated otherwise, the initial conditions are small random noises for the order parameter components, which represents a system quenched from high temperatures. Periodic boundary conditions are applied along the three directions.

The predicted domain structures along the basal plane (the *xy* plane) and 3D spaces are plotted in Figs. 1(a) and 1(b), in strikingly good agreement with those observed in experimental measurements [9,15,27]. As shown in Fig. 1(a), six domains meet together at the vortex and anti-vortex cores, which are the topological defects [8]. The 3D domain structures in Fig. 1(b) exhibit an anisotropic property, i.e., the *xy* plane shows more vortex cores than the *xz* and *yz* planes. The anisotropy is specific to the hexagonal system, whose property within the basal plane is typically different from that along the *z* axis, and the anisotropy is reflected by the anisotropic gradient energy coefficients in Eq. (1) with $s_Q^z > s_Q^x$ [10]. Thus the domain structures in Fig. 1(b) can reduce the interfacial energy, by avoiding domain walls perpendicular to the *z* axis. The distribution of vortex cores in the 3D space results in vortex line networks, and Fig. 1(c) shows the vortex lines corresponding to the domain structures in Fig. 1(b). Some vortex lines form loops inside the sample, whereas others go through the sample following the periodic boundary conditions [16,28]. The vortex lines in Fig. 1(c) tend to be parallel to the *z* direction, consistent with the anisotropic domain structures in Fig. 1(b) [29,30].

With the gradient energy coefficients obtained from first-principles calculations, the phase-field models can be employed to estimate the size of the vortex cores. As shown in Figs.

2(a) and 2(b), six domains converge to a point in the basal plane, with a decreasing magnitude of the structural order parameter, which is consistent with the claim of a real vortex in earlier experimental reports [15,25]. Note that the magnitude Q only depends on the distance to the center point, i.e., the vortex core region adopt the continuous U(1) symmetry. The vortex cores have a diameter of ~ 0.49 nm [Fig. S2], smaller than the experimental values of ~ 4-5 nm [15,25]. Note that there exist two types of domain walls in *h*-$YMnO_3$, i.e., sharp walls and 2/*c* walls [31,32], and the domain wall width of the 2/*c* type is larger than that of the sharp type. The theoretical domain wall width based on the parameter setting is ~0.5 nm (See supplemental Fig. S1 [22]), close to the sharp walls [10], whereas the experimental domain wall width is ~4 nm, close to the 2/*c* wall [25,31]. The difference of the domain wall width may lead to the difference in the vortex core size. Also, experimentally other structural and chemical defects may be concentrated near the vortex cores, which may increase the vortex core size.

The simulations indicate that the vortex cores are in the high-symmetry paraelectric phase with $Q \sim 0$ and $P \sim 0$, and the physical implication is demonstrated in Figs. 2 (c) and 2(d). The paraelectric nature of the vortex core is also discussed based on direct first-principles calculations [31]. The core structures of the structural topological defects, with the reduced magnitude of Q, are different from those of spin vortices, e.g., magnetic skyrmions, where the spins generally maintain the magnitude [33].

Pairs of vortex and anti-vortex can be annihilated to reduce the total interfacial energy at high temperatures in experiments [19], and here we investigate the annihilation process by phase-field simulations. As shown in Figs. 3(a) and 3(b), firstly the vortex and anti-vortex cores approach to each other, with decreased magnitude Q between the cores. The vortex and anti-vortex cores then coalesce to one point, as illustrated in Fig. 3(c). The stage is in the critical state,

i.e., the transient state between two topological defects and zero topological defects. The point is no longer topologically protected, since the six domains around it belong to four types of domains variants, rather than six types of domains. Afterwards, the shape of deep valley disappears and striped domains are formed, as shown in Fig. 3(d). The domain patterns obtained from the simulations is consistent with those observed experimentally, as demonstrated in Supplementary Fig. S3 [22].

In 3D spaces, the vortex-antivortex annihilation gives rise to the topological changes of the vortex lines, and the evolution starting from small random noises is shown in Supplementary Movie 1 [22]. We find that the evolution of vortex line loops consists of three basic topological changes, i.e., shrinking, coalescence, and splitting of vortex line loops. To demonstrate the three topological changes, we run the simulations using the isotropic gradient energy coefficients ($s_Q^z = s_Q^x$). Note that changing to isotropic gradient energy coefficients will not affect the topological changes.

With the isotropic gradient energy coefficients, the evolution of vortex line loops starting from three different initial configurations is demonstrated in Supplementary Movies 2-4 [22], and three snapshots are chosen for each movie, as shown in Fig. 4. If the system contains an isolated circular loop, the loop tends to shrink and disappear to reduce the interfacial energy [Figs. 4(a)-4(c)]. When two loop segments, as arcs of two circles with different centers, are close to each other, the two loop segments may exchange parts of them. If the two loop segments initially belong to different loops, the exchange leads to coalescence of the two loops, as shown in Figs. 4(d)-4(f). On the other hand, if the two loop segments are initially parts of one loop, the exchange results in the splitting of the loop into two loops, as shown in Figs. 4(g)-4(i). During

the three topological changes, the numbers of vortex line loops change from 1 to 0, 2 to 1, and 1 to 2, respectively, i.e., the numbers of vortex line loops are increased or decreased by 1. The evolution of the corresponding domain structures is provided in Supplementary Movies 5-7 [22]. From Movies 5-7, the shrinking of vortex line loops is caused by the shrinking of the domains within the loop, whereas the coalescence and splitting of vortex line loops are accompanied by the coalescence and splitting of related domains. Note that annihilation of vortex and anti-vortex can be observed on certain 2D planes in the three movies, e.g., on the *yz* plane going through the centers in Movie 6.

The evolution of the vortex lines behaves similar to that of the 3D lattice dislocation networks, where the dislocations with opposite Burgers vectors can be annihilated and dislocation loops can shrink [34,35]. The exchange of vortex line loops is analogous to the crossing of two disclinations in nematic liquid crystals, where the number of disclinations can increase or decrease by one [36,37]. Physically, the vortex lines in *h*-$REMnO_3$, dislocations, and disclinations are all 1D topological defects [1].

Next we focus on the scaling dynamics during the vortex-antivortex annihilation process. The scaling hypothesis claims that at late stages, the statistics of domain structures is independent of time while the characteristic length scales with time. It is known that the isotropic 3D XY model shows a power-law ordering kinetics, i.e., the vortex density ρ is a function of simulation steps t as: $\rho \sim 1/t$, whereas the 2D XY model exhibits the power-law with a logarithmic correction as expressed by $\rho \ln \rho \sim 1/t$ [38,39]. This is because the 2D XY model shows a slower coarsening dynamics, which originates from the scale-dependent friction constant [38,40,41].

In the 2D simulations of *h*-$YMnO_3$ on the basal plane, the average area of the domains *A*, with $A \sim 1/\rho$, is calculated as a function of simulation steps, i.e., time *t*. Also, the results from the 2D XY model are demonstrated for comparison (sixth order coefficients and polarization in Eq. 1 are set to zero). As shown in Fig. 5(a), the exponent of the average area *A* with respect to time *t* at late stages is about 0.87 and 0.86 for $YMnO_3$ and the XY model, respectively, different from the exponent of 1.00 in the 3D XY model and grain growth models [17,39]. After considering the logarithmic correction, the exponents are both 0.96, which is consistent with the analytical predictions of the 2D XY model [38,39]. This indicates that the annihilation of vortices and anti-vortices controls the coarsening process of the vortex state, and the 6-fold degeneracy does not significantly change the scaling behavior, although the 6-fold degeneracy results in the existence of domain walls. During the coarsening process, the domain walls tend to reduce their curvature, and the curvature-driven process is faster than the vortex-antivortex annihilation [38], as demonstrated in Supplementary Movie 8 [22]. As a reference, we also provide the evolution of domain structures for the XY model in Supplementary Movie 9 [22].

The results of 3D simulations with the anisotropic gradient energy coefficients are plotted in Fig. 5(b), and a yellow line with slope ~ -1.0 is drawn as the reference. The simulation data for *h*-$YMnO_3$ are parallel to the yellow line at small number of simulation steps, whereas deviates from the yellow line for large number of simulation steps. To reveal the origin of the deviation, we run the simulations using the isotropic gradient energy coefficients ($s_Q^z = s_Q^x$) with all the other simulation conditions unchanged, and the results are well fitted by the yellow line, as shown in Fig. 5(b). Thus the simulation results with the isotropic gradient energy coefficients are consistent with the prediction of the isotropic 3D XY model, and the deviation of $YMnO_3$ arises

from the anisotropic gradient energy coefficients ($s_Q^z > s_Q^x$). At large number of simulation steps, the order parameters are basically homogeneous along the z axis as shown in Fig. 2 (b), and the coarsening process becomes 2D-like with the exponent of -0.87 (a 2D system can be regarded as homogeneous along the z axis with $s_Q^z \to \infty$). Therefore, due to the anisotropy intrinsic to the hexagonal system, the scaling dynamics shows a crossover from 3D-like to 2D-like behaviors.

The scaling dynamics here is different from the Kibble–Zurek mechanism reported earlier [16]. The Kibble–Zurek mechanism applies to the situation of slow cooling with different cooling rates, and is based on the critical scaling analysis above the critical point [42-44]. The scaling dynamics here, on the other hand, corresponds to the phase-ordering dynamics at a specific temperature, after an infinitely rapid quench from high temperatures [38,43]. The Kibble-Zurek mechanism predicts that the vortex density follows a power-law with the exponent of ~0.57 with respect to different cooling rates [16], whereas the coarsening dynamics here gives rise to a curve with the slope ranging from -0.87 to -1.02 in the log-log plot, as shown in Fig. 5(b).

In summary, first-principles informed phase-field simulations of the vortex line network evolution in *h*-$REMnO_3$ reveals the dislocation-like topological changes, i.e., vortex line loop shrinking, coalescence, and splitting, as well as loop interactions and exchanges leading to the coalescence and splitting of domains. It is shown that the domains coarsen with time exhibits a power-law with a logarithmic correction, which indicates that the scaling dynamics is controlled by the vortex-antivortex annihilation rather than the movement of domain walls. The topological evolution mechanisms discovered here could be extended to different systems with line defects.

Acknowledgement:

The work at Penn State is supported by the Penn State MRSEC, Center for Nanoscale Science, under the award NSF DMR-1420620 (FX) and the U.S. Department of Energy, Office of Basic Energy Sciences, Division of Materials Sciences and Engineering under Award FG02-07ER46417 (FX and LQC). The work at Penn State used the Extreme Science and Engineering Discovery Environment (XSEDE), which is supported by National Science Foundation grant number ACI-1053575 [45]. The work at Rutgers is funded by the Gordon and Betty Moore Foundation's EPiQS Initiative through Grant GBMF4413 to the Rutgers Center for Emergent Materials. X.W. acknowledges the National Natural Science Foundation of China (Grant No. 11604011).

References

[1] P. M. Chaikin and T. C. Lubensky, *Principles of condensed matter physics* (Cambridge Univ Press, 2000), Vol. 1.
[2] N. D. Mermin, Reviews of Modern Physics **51**, 591 (1979).
[3] M. Cruz, N. Turok, P. Vielva, E. Martinez-Gonzalez, and M. Hobson, Science **318**, 1612 (2007).
[4] D. S. Fisher, M. P. A. Fisher, and D. A. Huse, Physical Review B **43**, 130 (1991).
[5] G. P. Alexander, B. G.-g. Chen, E. A. Matsumoto, and R. D. Kamien, Reviews of Modern Physics **84**, 497 (2012).
[6] F. T. Huang and S. W. Cheong, Nature Reviews Materials **2**, 17004 (2017).
[7] J. M. Kosterlitz and D. J. Thouless, Journal of Physics C: Solid State Physics **6**, 1181 (1973).
[8] T. Choi, Y. Horibe, H. Yi, Y. Choi, W. Wu, and S.-W. Cheong, Nature materials **9**, 253 (2010).
[9] S. Chae, Y. Horibe, D. Jeong, S. Rodan, N. Lee, and S.-W. Cheong, Proceedings of the National Academy of Sciences **107**, 21366 (2010).
[10] S. Artyukhin, K. T. Delaney, N. A. Spaldin, and M. Mostovoy, Nature materials **13**, 42 (2013).
[11] C. J. Fennie and K. M. Rabe, Physical Review B **72**, 100103 (2005).
[12] B. B. Van Aken, T. T. Palstra, A. Filippetti, and N. A. Spaldin, Nature materials **3**, 164 (2004).

[13] T. Lonkai, D. G. Tomuta, U. Amann, J. Ihringer, R. W. A. Hendrikx, D. M. Többens, and J. A. Mydosh, Physical Review B **69**, 134108 (2004).
[14] A. S. Gibbs, K. S. Knight, and P. Lightfoot, Physical Review B **83**, 094111 (2011).
[15] Q. Zhang, G. Tan, L. Gu, Y. Yao, C. Jin, Y. Wang, X. Duan, and R. Yu, Scientific reports **3**, 2741 (2013).
[16] S.-Z. Lin *et al.*, Nature Physics **10**, 970 (2014).
[17] L.-Q. Chen and W. Yang, Physical Review B **50**, 15752 (1994).
[18] F. Xue, X. Wang, Y. Gu, L.-Q. Chen, and S.-W. Cheong, Scientific reports **5**, 17057 (2015).
[19] S. C. Chae, N. Lee, Y. Horibe, M. Tanimura, S. Mori, B. Gao, S. Carr, and S.-W. Cheong, Physical review letters **108**, 167603 (2012).
[20] D. M. Hatch and H. T. Stokes, Journal of applied crystallography **36**, 951 (2003).
[21] A. Tagantsev, Ferroelectrics **69**, 321 (1986).
[22] See Supplemental Material at [URL will be inserted by publisher] for validation of the modification of the gradient energy coefficient, analysis of the vortex core size in the basal plane, vortex-antivortex annihilation, and movies for 1: evolution of vortex lines starting from small random noises, 2-4: vortex line loop shrinking, coalescence, and splitting, 5-7: evolution of domain structures during the vortex line loop shrinking, coalescence, and splitting, and 8-9: evolution of 2D domain structures for $YMnO_3$ and XY model.
[23] L.-Q. Chen and J. Shen, Computer Physics Communications **108**, 147 (1998).
[24] F. Xue, X. Wang, Y. Shi, S.-W. Cheong, and L.-Q. Chen, Physical Review B **96**, 104109 (2017).
[25] J. Li, F.-K. Chiang, Z. Chen, C. Ma, M.-W. Chu, C.-H. Chen, H. Tian, H. Yang, and J. Li, Scientific reports **6**, 28047 (2016).
[26] G. Rupprecht and R. Bell, Physical Review **135**, A748 (1964).
[27] S. M. Griffin, M. Lilienblum, K. T. Delaney, Y. Kumagai, M. Fiebig, and N. A. Spaldin, Physical Review X **2**, 041022 (2012).
[28] D. A. Garanin, E. M. Chudnovsky, and T. Proctor, Physical Review B **88**, 224418 (2013).
[29] W. Janke and T. Matsui, Physical Review B **42**, 10673 (1990).
[30] S. R. Shenoy and B. Chattopadhyay, Physical Review B **51**, 9129 (1995).
[31] Y. Kumagai and N. A. Spaldin, Nature communications **4**, 1540 (2013).
[32] Q. H. Zhang *et al.*, Physical Review B **85**, 020102 (2012).
[33] N. Romming, C. Hanneken, M. Menzel, J. E. Bickel, B. Wolter, K. von Bergmann, A. Kubetzka, and R. Wiesendanger, science **341**, 636 (2013).
[34] C. Shen and Y. Wang, Acta Materialia **51**, 2595 (2003).
[35] S. H. Haghighat, G. Eggeler, and D. Raabe, Acta Materialia **61**, 3709 (2013).
[36] S. Copar and S. Zumer, Physical review letters **106**, 177801 (2011).
[37] I. Chuang, B. Yurke, A. N. Pargellis, and N. Turok, Physical Review E **47**, 3343 (1993).
[38] A. J. Bray, Advances in Physics **43**, 357 (1994).
[39] B. Yurke, A. N. Pargellis, T. Kovacs, and D. A. Huse, Physical Review E **47**, 1525 (1993).
[40] A. N. Pargellis, P. Finn, J. W. Goodby, P. Panizza, B. Yurke, and P. E. Cladis, Physical Review A **46**, 7765 (1992).
[41] A. Pargellis, N. Turok, and B. Yurke, Physical review letters **67**, 1570 (1991).
[42] W. Zurek, Nature **317**, 505 (1985).
[43] A. Jelić and L. F. Cugliandolo, Journal of Statistical Mechanics: Theory and Experiment **2011**, P02032 (2011).
[44] W. H. Zurek, U. Dorner, and P. Zoller, Physical review letters **95**, 105701 (2005).
[45] J. Towns *et al.*, Computing in Science & Engineering **16**, 62 (2014).

Figure Legends

Fig. 1. 2D and 3D domain configurations. (a) Part of the domain structures from a 2D simulation on the basal plane with a system size of $1024\Delta x \times 1024\Delta x \times 1\Delta x$ and grid spacing of $\Delta x = 0.30\ nm$. The six colors represent six types of domains. (b) Domain structures from a 3D simulation with a system size of $128\Delta x \times 128\Delta x \times 128\Delta x$ and grid spacing of $\Delta x = 0.30\ nm$. (c) Vortex lines in 3D spaces corresponding to the domain structures in (b). The brown dots denote the intersection of vortex lines and surfaces.

Fig. 2. Demonstration of vortex core structures. (a) and (b) Distribution of the structural trimerization magnitude *Q* near a vortex core and an anti-vortex core, respectively. The domain structures are from 2D simulations on the basal plane with grid spacing of $\Delta x = 0.020\ nm$, and the height represents the value of *Q* with the equilibrium bulk value of 9.5×10^{-2} *nm*. (c) and (d) The corresponding atomic structures near a vortex core and an anti-vortex core, respectively. The vortex cores have a size of about one unit cell, and show the paraelectric phase with $Q \sim 0$. The red arrows in (c) and (d) represent the displacement directions of oxygen atoms.

Fig. 3. Evolution of vortex structures during vortex-antivortex annihilation. (a)-(d) Vortex structures at different simulation time steps. The simulation is on the 2D basal plane and the height represents the magnitude of the structural order parameter *Q*. In (c) the two red domains are connected by a point with Q~0, and the point separates the two light blue domains as well.

Fig. 4. Topological evolution of vortex lines. (a)-(c) Shrinking, (d)-(f) coalescence, and (g)-(i) splitting of vortex line loops.

Fig. 5. 2D and 3D coarsening dynamics. (a) Average domain area as a function of simulation steps in the 2D basal plane. The squares and circles correspond to the raw data and the data with logarithmic correlations, respectively. Different lines are fitted based on the formula: $a + t^b$. (b) Total vortex line length as a function of simulation steps in 3D simulations. The pink squares correspond to the anisotropic gradient coefficients. The yellow circles are results using the isotropic gradient coefficients as the control experiments, which are fitted by a yellow line. (a) is the average result of five parallel simulations with a system size of $2048\Delta x \times 2048\Delta x \times 1\Delta x$ and grid spacing of $\Delta x = 0.30\ nm$, and (b) is the average of three parallel simulations with a system size of $512\Delta x \times 512\Delta x \times 512\Delta x$ and grid spacing of $\Delta x = 0.30\ nm$.

Figure 1

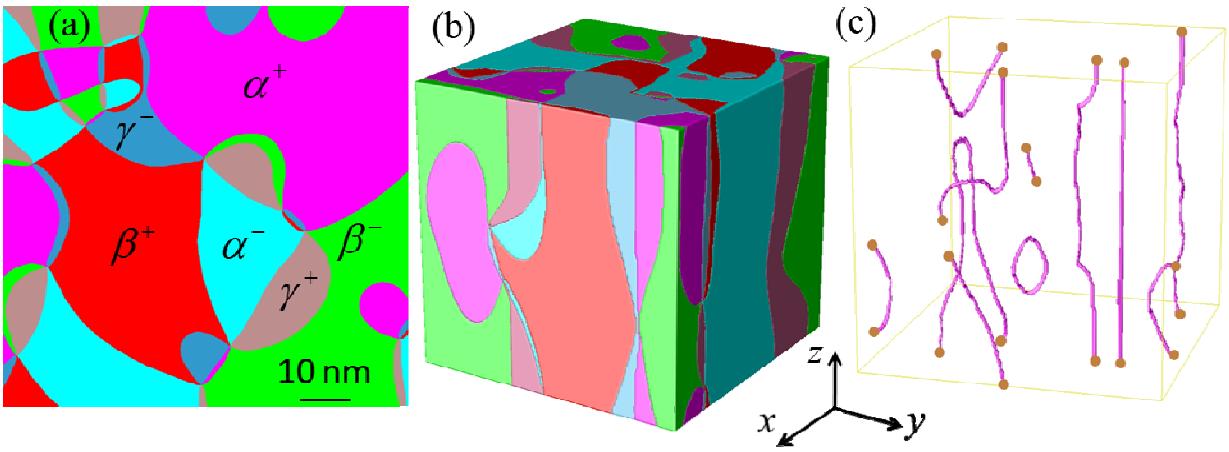

Figure 2

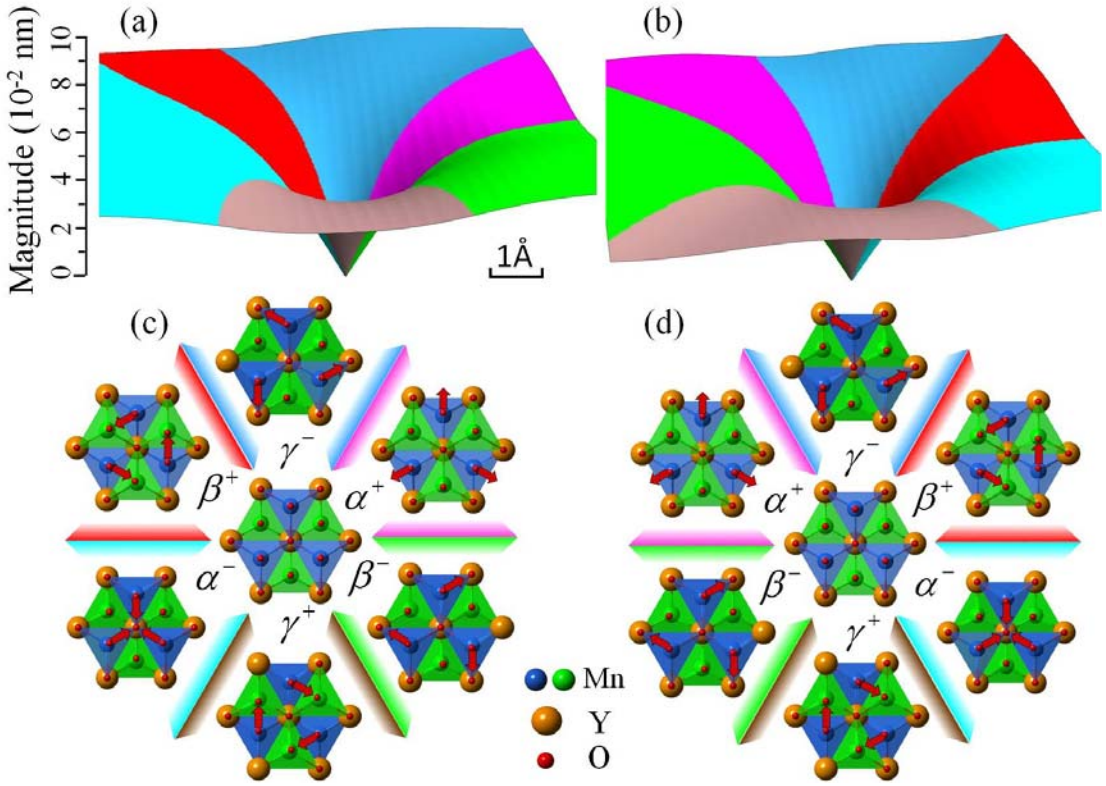
(a)
(b)
Magnitude (10^{-2} nm)
0 2 4 6 8 10
1Å
(c)
(d)
γ^-
β^+
α^+
α^-
β^-
γ^+
Mn
Y
O

Figure 3

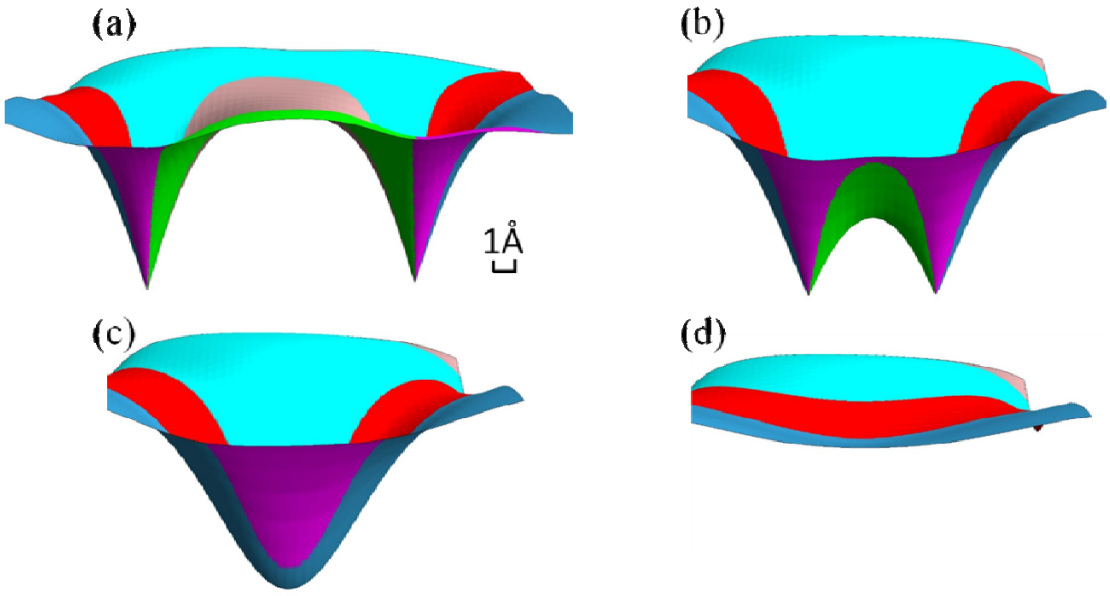

Figure 4

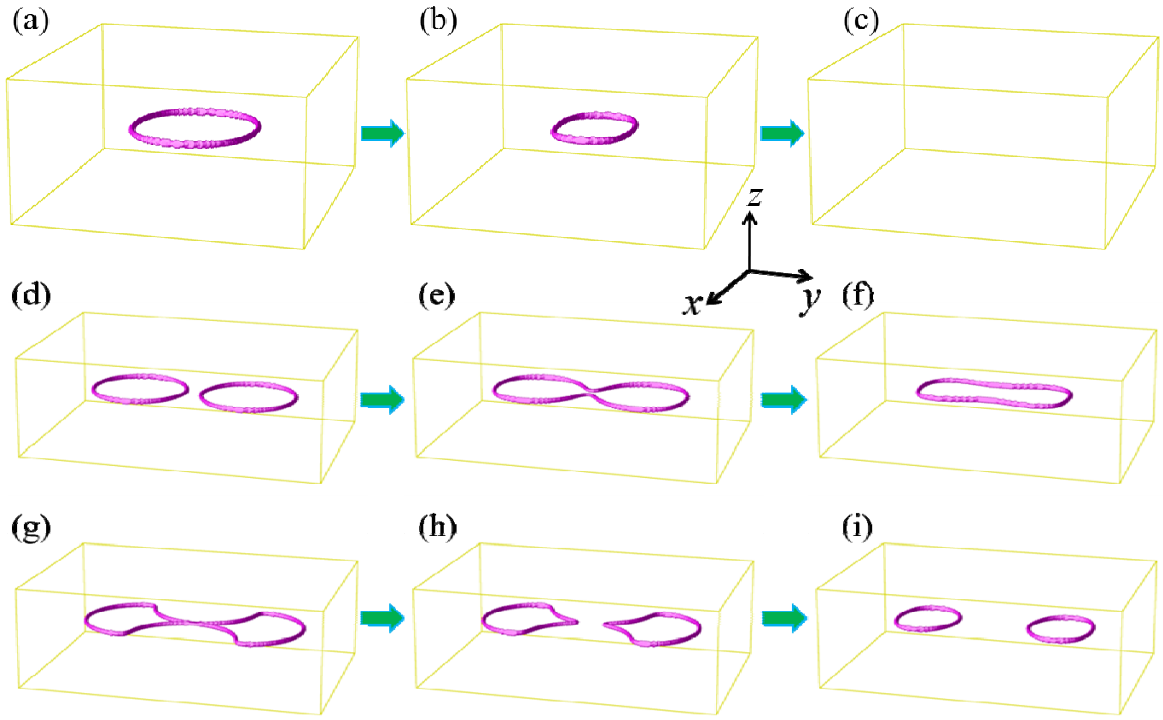

Figure 5

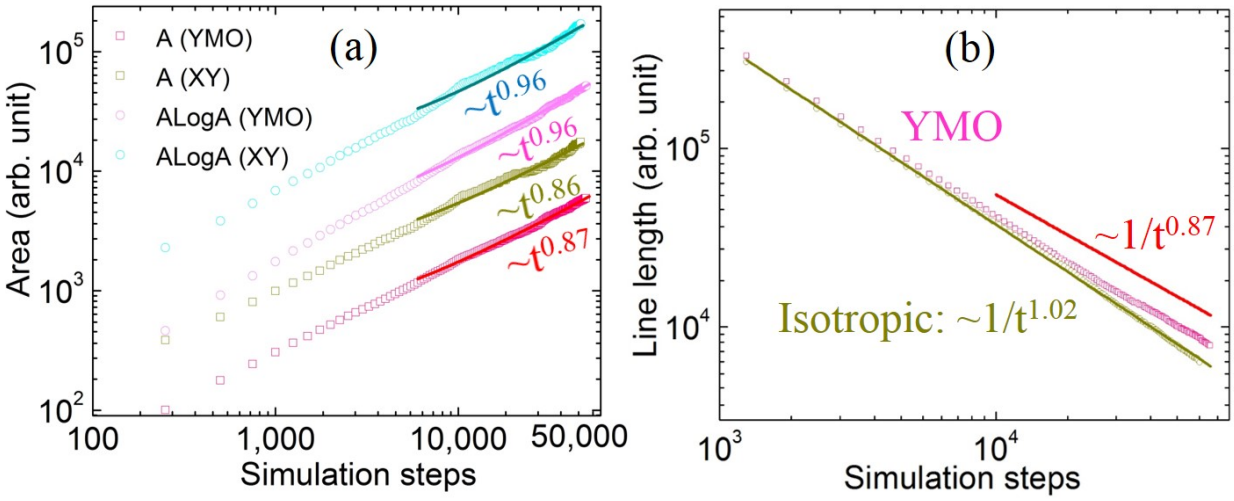
A (YMO)
A (XY)
ALogA (YMO)
ALogA (XY)
(a)
~t^0.96
~t^0.96
~t^0.86
~t^0.87
Area (arb. unit)
Simulation steps
(b)
YMO
~1/t^0.87
Isotropic: ~1/t^1.02
Line length (arb. unit)
Simulation steps